

# Model-based Digital Image Correlation for Non-contact Deformation Measurement of Strain Field and Mechanical Property

Yang Huang, Jingjing Ji, *Member, IEEE*, Kok-Meng Lee, *Fellow, IEEE*

**Abstract**—This paper presents a new method that combines a physics-based model and finite-element (FE)-based digital image correlation (DIC) with an interfacial continuity condition for simultaneous deformation measurements of strain field and material mechanical properties. The dual-domain global DIC method incorporates a model-based kernel that offers useful physical insights into the complex deformation and constrains the solutions to the iterative minimization of the DIC criterion, which leads to a faster convergence. Unlike local subset-based and global FE-based methods where the DIC is formulated to solve for the nodal displacements, the model-based DIC that accounts for complex deformation in the specific region is formulated to identify system parameters. Both domains, along with their interface and the continuity condition enforced on the global displacement field, are discretized and solved simultaneously in a single calculation. The dual-domain global DIC method has been investigated by comparing reconstructed strain fields and estimated parameters against targets simulated using the commercial FEA software COMSOL and published experimental data. Unlike FE-DIC which is noise sensitive, the model-based DIC is robust against the Gaussian noise effects.

**Index Terms**— Deformation measurement, digital image correlation, parameter identification, field reconstruction

## I. INTRODUCTION

As a full-field technique for shape, motion and deformation measurement [1], digital image correlation (DIC) has been widely utilized in process monitoring [2], mechanical response analyze [3], and damage/flaw evolution tracking [4]. DIC analyzes material surface textures or artificial speckle patterns between two images, typically a reference (previous) image and a target (current) image, to determine their relative displacement, thus offering a non-contact and non-intrusive measurement with high efficiency [5]. Provided that the deforming material is properly patterned and well imaged, DIC methods are capable of measuring deformations in multi-length-scale ranging from meters to nanometers with different materials such as metal alloys [6], polymers [7] and more recently, bio-tissues [8].

DIC methods are increasingly used in experimental mechanics to characterize models as well as to validate FE analyses. Existing research and applications so far, however,

This work was supported by the National Science Foundation of China under Grant 51505168 and U1713204, in part by U.S. National Science Foundation under Grant CMMI-1662700.

Yang Huang, Jingjing Ji and Kok-Meng Lee are with the State Key Lab of Digi. Manuf. Equip. and Tech., Huazhong Univ. of Sci. and Tech., Wuhan 430074, China. Kok-Meng Lee is Professor of Mech. Eng., Georgia Inst. of Tech., Atlanta, GA 30332 USA.

\*Corresponding authors: [jijingjing@hust.edu.cn](mailto:jijingjing@hust.edu.cn), [kokmeng.lee@me.gatech.edu](mailto:kokmeng.lee@me.gatech.edu).

primarily focus on developing different correlation criterion algorithms and displacement descriptions [9] to obtain accurate strain measurements. Their abilities for simultaneous rapid measurements of geometric-based variables (such as displacement and strain) and parameter identification of material (mechanical) properties are under exploited.

Two most commonly used DIC algorithms are the subset-based local DIC and the finite-element (FE) based global DIC. Local DIC allocates separate reference subset centered at each calculation point and then traces the corresponding deformed subset in target images by correlating between two images [10]. Unlike local DIC (without enforcing the displacement continuity to the displacement field), global DIC discretizes the whole surface into FEs and traces all the nodal displacements simultaneously in a single calculation [11]. The displacement measurements have been theoretically and experimentally validated for both local and global DIC [12]; and material properties can be identified by additional numerical simulations with DIC measurements through an inverse technique [13]. When encountering applications that involve complex or large localized deformation, both existing subset-based local DIC and FE-based global DIC suffer several drawbacks: the independent calculated solutions in local DIC fail to satisfy the continuity condition to maintain the global displacement field. For global DIC, high-order FE shape functions [14] or adaptive re-mesh strategies [15] for capturing complex deformation fields are computationally demanding along with clumsy formulations, but there are tradeoffs between resolution and accuracy as large elements tend to improve accuracy but at the expense of resolution [16].

Recent technologically advancing applications (such as additive-manufacturing that requires quantitative assessments of the process-induced stress between each built layers [17]) motivates the development of improved DIC methods for analyzing complex deformation in specific local regions or at interfaces in images. In [18], mechanically aided equilibrium condition was introduced as a regularization term in a DIC algorithm to improve accuracy but the added regularization process requires extra computation undesirable for real-time implementation. Physics-based models are commonly coupled in image processing to obtain high fidelity in applications; object recognition [19], image segmentation [20], and more recently nanoscale deformation analysis with high-resolution transmission electron microscopy images with DIC [21].

With global DIC as a field measurement tool, this paper presents a dual-domain (model- and FE-based) DIC method for simultaneous reconstruction of displacement/strain fields and

identification of material properties. The remainder of this paper offers the followings:

- The dual-domain global DIC, which combines a physics-based model and FE-based DIC with an interfacial continuity condition, is formulated. As will be shown by comparing to two existing approaches (FE-based DIC and general global DIC), the model-based DIC that accounts for the physics of complex deformation through identifying the system parameters provides an efficient means to constrain the solutions to the iterative minimization of the DIC criterion leading to a faster convergence.
- With two examples (rigid-body translation and uniaxial tensile loading) where solutions are available for validation, the dual-domain global DIC method utilizing a model-kernel is numerically illustrated. The effects of FE sizes, intensity changes and random noise on the measuring accuracy, computation time and robustness of the DIC are discussed.
- The model-based enhancements are validated by comparing the DIC-reconstructed displacement/strain fields against FEA simulation targets. The effectiveness of the verified dual-domain method is further demonstrated by evaluating the DIC-reconstructed fields and estimated parameters with published experimental data.

## II. MODEL-BASED DUAL-DOMAIN DIC

Consider a 2D deformation of an interested subset in two consecutive images as illustrated in Fig. 1 where the parameters involved in measuring the deformation behavior of the material are shown. In Fig. 1(a),  $\mathbf{u}(s) = [u \ v]^T$  is the displacement of the subset centered at  $A$  where the set of the points is assumed to remain as its neighboring points. When the subset is sufficiently small, each of the points (denoted by its location  $\mathbf{s}_i = [x_i \ y_i]^T$ ) around the subset center  $A$  in the previous image is mapped to that in the current image according to the relation  $\tilde{\mathbf{s}} = \mathbf{s} + \mathbf{u} + \nabla \mathbf{u} [\Delta x \ \Delta y]^T$ . The objective is to estimate the displacement field  $\mathbf{u}$  from the sequential images so that the Green-Lagrange strain tensor can be determined.

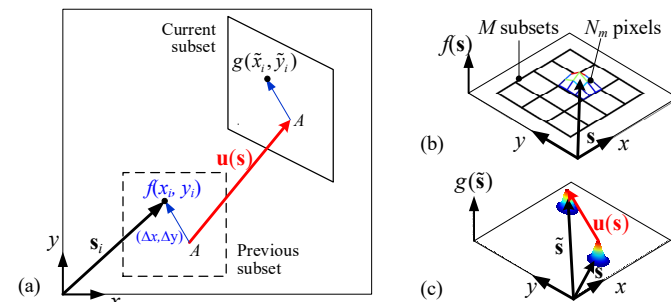


Fig.1 Schematics illustrating DIC (a) Displacement reference and deformed subsets. (b) Previous image. (c) Current image.

As shown in Fig. 1(b), the image is discretized into  $M$  subsets ( $m \in [1, M]$ ) and  $N_m$  is the total number of pixels in the  $m^{\text{th}}$  subset ( $n \in [1, N_m]$ ). Let  $f(\mathbf{s})$  and  $g(\tilde{\mathbf{s}})$  represent the gray intensity distribution of the previous and current subsets (Fig. 1c) respectively. Using a first-order Taylor approximation,

$$g(\tilde{\mathbf{s}}) \approx g(\mathbf{s}) + \mathbf{u}^T \nabla g \quad (1)$$

In (1),  $\nabla g$  is the gradient with respect to  $\mathbf{s}$ . In a two-dimension (2D) DIC analysis, the displacement field  $\mathbf{u}$  is obtained by evaluating the similarity degree between the two sequential images. Equation (2a) describes the least-square correlation criterion for estimating the global residual:

$$R_c(\mathbf{u}) = \sum_{m=1}^M [f_m(\mathbf{s}) - g_m(\tilde{\mathbf{s}})]^2 \quad (2a)$$

$$\text{where } f_m(\mathbf{s}) = \frac{f(\mathbf{s}) - \bar{f}_m}{\bar{f}_m}; \quad g_m(\tilde{\mathbf{s}}) = \frac{g(\tilde{\mathbf{s}}) - \bar{g}_m}{\bar{g}_m}; \quad (2b, c)$$

( $\bar{f}_m, \bar{f}_m$ ) and ( $\bar{g}_m, \bar{g}_m$ ) are the ensemble (average, root-sum-square) of the previous and current subsets, respectively:

$$\bar{f}_m = \frac{1}{N_m} \sum_{n=1}^{N_m} f(\mathbf{s}_n); \quad \bar{f}_m = \sqrt{\sum_{n=1}^{N_m} [f(\mathbf{s}_n) - \bar{f}_m]^2} \quad (3a, b)$$

$$\bar{g}_m = \frac{1}{N_m} \sum_{n=1}^{N_m} g(\tilde{\mathbf{s}}_n); \quad \bar{g}_m = \sqrt{\sum_{n=1}^{N_m} [g(\tilde{\mathbf{s}}_n) - \bar{g}_m]^2} \quad (3c, d)$$

By subtracting the mean value and dividing the root-sum-square of the subset, the correlation criteria (2a) is insensitive to offset and scale changes in the intensity of the current image [22] to provide an accurate and reliable estimation of the displacement.

The displacement field  $\mathbf{u}(\mathbf{s})$  is commonly described by means of a global FE method. Fig. 2(a) shows an illustration where quadrilateral elements with linear shape functions are used:

$$\mathbf{u}(\mathbf{s}_i) = \sum_{q=1}^l (\psi_q(\mathbf{s}_i) \mathbf{u}_q) \quad (4)$$

In (4),  $\psi_q(\mathbf{s})$  is a FE shape-function where  $q=1, 2, \dots, l$  for an element of  $l$  nodes (where  $l$  is a multiple of 4).

$$\psi_1 = (1 - \xi)(1 - \eta); \quad \psi_2 = \xi(1 - \eta); \quad \psi_3 = \xi\eta; \quad \psi_4 = (1 - \xi)\eta$$

$$\text{where } \sum_{q=1}^4 \psi_q = 1; \quad \xi \in [0, 1]; \quad \eta \in [0, 1].$$

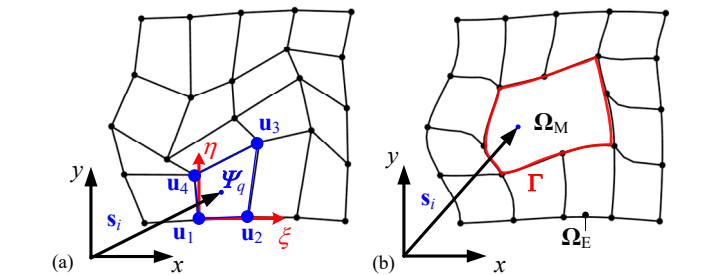


Fig.2 Displacement field formulation. (a) FE domain  $\Omega_E$ . (b) Model-based domain  $\Omega_M$ .

### A. Dual-domain formulation of displacement field

A dual domain formulation is proposed as shown in Fig. 2(b) to overcome the problems associated with the global FE method (Fig. 2a) where the displacement field  $\mathbf{u}(\mathbf{s})$  is divided into FE based domain  $\Omega_E$  as in (4) and a model-based  $\Omega_M$  domain:

$$\mathbf{u}(\mathbf{s}_i) = \begin{cases} \mathbf{u}_M(\mathbf{s}_i) & \text{for } \mathbf{s}_i \in \Omega_M \\ \mathbf{u}_E(\mathbf{s}_i) & \text{for } \mathbf{s}_i \in \Omega_E \end{cases} \quad (5a)$$

$$\text{where } \mathbf{u}_M(\mathbf{s}_i) = \mathbf{H}_M(\mathbf{s}_i) \boldsymbol{\alpha}; \quad \mathbf{u}_E(\mathbf{s}_i) = \mathbf{H}_E(\mathbf{s}_i) \boldsymbol{\beta}; \quad (5b, c)$$

$$\boldsymbol{\alpha} (\in R^{n_M \times 1}) = [\alpha_1 \ \cdots \alpha_j \ \cdots \ \alpha_{n_M}]^T; \text{ and}$$

$$\boldsymbol{\beta} (\in R^{2l \times 1}) = [\mathbf{u}_1^T \ \cdots \mathbf{u}_q^T \ \cdots \ \mathbf{u}_{2l}^T]^T.$$

In (5a), the model-kernel  $\mathbf{H}_M$  ( $\in R^{2 \times n_M}$ ) that depends on specific applications take advantages of prior physical information of the deformation field; and  $\mathbf{H}_E$  ( $\in R^{2 \times 2l}$ ) is defined by (4). The formulation and its significance are illustrated with an example; complex deformation under uniaxial tension (Fig. 3).

*Example: Complex deformation under uniaxial tension*

Fig. 3 shows a thin symmetrical plate (Young's modulus  $E$  and Poisson ratio  $\nu$ ) with a circular through-hole (radius  $a$ ) under uniaxial tensile loading  $T$ , where theoretical solutions to its displacement field in isotropic infinite plate indicate the trend of the physical deformation. In polar coordinates [23],

$$\frac{u(r, \theta)}{Ta/E} = \frac{(a^3 - ar^2)(\nu + 1)}{2r^3} C_{3\theta} - \frac{a^2(\nu - 1) + r^2\nu}{ar} C_\theta \quad (6a)$$

$$\frac{v(r, \theta)}{Ta/E} = \frac{(a^3 - ar^2)(\nu + 1)}{2r^3} S_{3\theta} + \frac{2a^2 + r^2}{ar} S_\theta \quad (6b)$$

In (6a, b),  $C_{(\bullet)}$  and  $S_{(\bullet)}$  denote  $\cos(\bullet)$  and  $\sin(\bullet)$  respectively. A model-based domain  $\Omega_M$  is defined to capture the deformation occurred around the hole. The corresponding displacement ( $\mathbf{s}_i \in \Omega_M$ ) is given in (5a) where

$$\mathbf{H}_M(R_i, \theta_i) = \begin{bmatrix} \frac{C_{3\theta_i}}{2R_i^3} - \frac{2C_{\theta_i} + C_{3\theta_i}}{2R_i} & \frac{C_{3\theta_i}}{2R_i^3} + \frac{2C_{\theta_i} - C_{3\theta_i}}{2R_i} - R_i C_{\theta_i} \\ \frac{S_{3\theta_i}}{2R_i^3} + \frac{4S_{\theta_i} - S_{3\theta_i}}{2R_i} + R_i S_{\theta_i} & \frac{S_{3\theta_i}}{2R_i^3} - \frac{S_{3\theta_i}}{2R_i} \end{bmatrix} \quad (7a)$$

$$\boldsymbol{\alpha} = \begin{bmatrix} \alpha_1 \\ \alpha_2 \end{bmatrix} \text{ where } \alpha_1 = \frac{Ta}{E}; \alpha_2 = \frac{Ta}{E}\nu; \quad (7b)$$

$$R_i = \frac{1}{a} \sqrt{x_i^2 + y_i^2}; \text{ and } \theta_i = \arctan\left(\frac{y_i}{x_i}\right). \quad (7c, d)$$

In (7a), the hole (center  $\mathbf{s}=0$  and radius  $a$ ) can be located using image processing such as Hough transform method. With (7a),  $\mathbf{H}_M(R_i, \theta_i)$  can be computed for the  $i^{\text{th}}$  pixel in  $\Omega_M$ , which provides the basis to solve (5a) for the unknown  $\boldsymbol{\alpha}$  defined in (7b). The formulation (5a) with estimated  $\mathbf{u}$  in  $\Omega_M$  has the following significances: 1) The material properties ( $E, \nu$ ) can be obtained from the solution to  $\boldsymbol{\alpha}$  for a specified  $T$ . 2) Alternatively,  $T$  can be determined if the  $(E, \nu)$  is known.

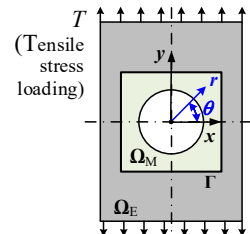


Fig. 3 Subdomains ( $\Omega_E$  and  $\Omega_M$ ) and parameters of model-based domain in uniaxial tension.

The displacements ( $\mathbf{u}_M$  and  $\mathbf{u}_E$ ) in the respective subdomains ( $\Omega_M$  and  $\Omega_E$ ) on the interface  $\Gamma$  must satisfy the continuity condition accounted for by the weak-form formulation in (8a) where  $\boldsymbol{\lambda} (\in R^{2 \times 1})$  is Lagrange multiplier [24]:

$$\sum_{\Gamma} \boldsymbol{\lambda}^T (\mathbf{u}_{M_i} - \mathbf{u}_{E_i}) = 0 \quad (8a)$$

In (8a), the interpolation of the Lagrange multiplier is written in

matrix form where  $\mathbf{H}_\Gamma \in R^{2 \times 2n_\Gamma}$  and  $\boldsymbol{\gamma} \in R^{2n_\Gamma \times 1}$ :

$$\boldsymbol{\lambda}(\mathbf{s}_i) = \mathbf{H}_\Gamma(\mathbf{s}_i) \boldsymbol{\gamma}. \quad (8b)$$

*B. DIC Solutions based on Gauss-Newton approach*

For the dual-domain displacement formulation (5a), the objective of the DIC algorithm is to find the displacements ( $\mathbf{u}_M$  and  $\mathbf{u}_E$ ) in the respective subdomains ( $\Omega_M$  and  $\Omega_E$ ) along with  $\boldsymbol{\lambda}$  in (8a) that satisfies the continuity condition at the interface to minimize  $R_c$  for the whole region [25].

$$\text{Minimize } R_c(\mathbf{u}_E) + R_c(\mathbf{u}_M) \text{ subject to (8a)} \quad (9)$$

To solve (9) for the displacement field, the Lagrange function defined in (10) is minimized using a Gauss-Newton iteration scheme (11a) where the subscripts,  $k$  and  $k+1$ , refer to old and new  $\mathbf{x} = [\mathbf{a}^T \quad \boldsymbol{\beta}^T \quad \boldsymbol{\gamma}^T]^T$  in each iteration:

$$L(\mathbf{x}) = R_c[\mathbf{u}_M(\boldsymbol{\alpha})] + R_c[\mathbf{u}_E(\boldsymbol{\beta})] + \sum_{\Gamma} \boldsymbol{\lambda}^T (\mathbf{u}_{M_i} - \mathbf{u}_{E_i}) \quad (10)$$

$$[\nabla \nabla L(\mathbf{x}_k)] \Delta \mathbf{x} = -\nabla L(\mathbf{x}_k) \quad (11a)$$

$$\mathbf{x}_{k+1} = \mathbf{x}_k + \Delta \mathbf{x} \quad (11b)$$

The gradient  $\nabla L$  with respect to each DOF can be derived from (1), (2a), (5a) and (8a) leading to (12a):

$$\nabla L(\mathbf{x}) = \begin{bmatrix} \partial_{\boldsymbol{\alpha}} L \\ \partial_{\boldsymbol{\beta}} L \\ \partial_{\boldsymbol{\gamma}} L \end{bmatrix} = \begin{bmatrix} \partial_{\boldsymbol{\alpha}} [R_c(\boldsymbol{\alpha})] + \sum_{\Gamma} \mathbf{H}_M^T \boldsymbol{\lambda} \\ \partial_{\boldsymbol{\beta}} [R_c(\boldsymbol{\beta})] - \sum_{\Gamma} \mathbf{H}_E^T \boldsymbol{\lambda} \\ \sum_{\Gamma} [\mathbf{H}_\Gamma^T (\mathbf{u}_{M_i} - \mathbf{u}_{E_i})] \end{bmatrix} = \begin{bmatrix} \mathbf{F}_+ \\ \mathbf{F}_- \\ \mathbf{F}_\Gamma \end{bmatrix} \quad (12a)$$

where  $\partial_{(\bullet)} = \partial / \partial (\bullet)$ ,  $\mathbf{H}_M^T (\in R^{n_M \times 2}) = \partial_{\boldsymbol{\alpha}} \mathbf{u}_M^T$ ,  $\mathbf{H}_E^T (\in R^{2l \times 2}) = \partial_{\boldsymbol{\beta}} \mathbf{u}_E^T$ ; and  $\mathbf{H}_\Gamma^T (\in R^{2n_\Gamma \times 2}) = \partial_{\boldsymbol{\gamma}} \boldsymbol{\lambda}^T$  are the coefficient matrices in (5a) and (8a) respectively. In (12a) where the subscripts “+” and “-” denote the subdomains ( $\Omega_M$  and  $\Omega_E$ ) respectively,

$$\mathbf{F}_{\pm} = \frac{-2}{\bar{g}_m} \sum_{\Omega_{\pm}} [f_m(\mathbf{s}) - g_m(\tilde{\mathbf{s}})] \mathbf{H}_{\pm}^T \nabla g \pm \sum_{\Gamma} \mathbf{H}_{\pm}^T \boldsymbol{\lambda} \quad (12b)$$

Thus,  $\nabla \nabla L$  is a square matrix ( $\in n_M + 2l + 2n_\Gamma$ ) of the form:

$$\nabla \nabla L(\mathbf{u}) = \begin{bmatrix} \partial_{\boldsymbol{\alpha}} (\partial_{\boldsymbol{\alpha}} L) & 0 & \partial_{\boldsymbol{\gamma}} (\partial_{\boldsymbol{\alpha}} L) \\ 0 & \partial_{\boldsymbol{\beta}} (\partial_{\boldsymbol{\beta}} L) & \partial_{\boldsymbol{\gamma}} (\partial_{\boldsymbol{\beta}} L) \\ \partial_{\boldsymbol{\alpha}} (\partial_{\boldsymbol{\gamma}} L) & \partial_{\boldsymbol{\beta}} (\partial_{\boldsymbol{\gamma}} L) & 0 \end{bmatrix} \quad (13)$$

With (12a), the Gaussian-Newton iteration (11a) can be written in compact form (14a~c) for updating the ( $n_M + 2l + 2n_\Gamma$ ) elements in  $\Delta \mathbf{x}$ :

$$\begin{bmatrix} \mathbf{K}_+ & \mathbf{0}_{n_M \times 2l} & \mathbf{C}_+ \\ \mathbf{0}_{2l \times n_M} & \mathbf{K}_- & -\mathbf{C}_- \\ \mathbf{C}_+^T & -\mathbf{C}_-^T & \mathbf{0}_{2n_\Gamma \times 2n_\Gamma} \end{bmatrix} \Delta \mathbf{x} = -\begin{bmatrix} \mathbf{F}_+ \\ \mathbf{F}_- \\ \mathbf{F}_\Gamma \end{bmatrix} \quad (14a)$$

$$\text{where } \mathbf{K}_{\pm} = \frac{2}{\bar{g}_m} \sum_{\Omega_{\pm}} \mathbf{H}_{\pm}^T (\nabla g) (\nabla g)^T \mathbf{H}_{\pm}; \quad (14b)$$

$$\text{and } \mathbf{C}_{\pm} = \sum_{\Gamma} \mathbf{H}_{\pm}^T \mathbf{H}_{\Gamma} \quad (14c)$$

*C. Procedure for calculating strain displacement field*

With the reconstructed displacement field  $\mathbf{u}$ , the Green-Lagrangian strain tensor can be determined from (15) where the subscripts ( $x$  and  $y$ ) of the displacements ( $u$  and  $v$ ) indicate their respective partial derivatives:

$$\boldsymbol{\varepsilon} = \begin{bmatrix} \varepsilon_x & \varepsilon_{xy} \\ \varepsilon_{xy} & \varepsilon_y \end{bmatrix} \quad (15a)$$

$$\text{where } \begin{bmatrix} \varepsilon_x \\ \varepsilon_y \\ \varepsilon_{xy} \end{bmatrix} = \frac{1}{2} \begin{bmatrix} 2+u_x & 0 & v_x & 0 \\ 0 & u_y & 0 & 2+v_y \\ u_y & 1 & 1 & v_x \end{bmatrix} \begin{bmatrix} u_x \\ u_y \\ v_x \\ v_y \end{bmatrix} \quad (15b)$$

To evaluate the (combined elastic and plastic) deformation state of the material, the Von Mises yield criterion is applied using the equivalent strain (16):

$$\varepsilon_{eq} = \sqrt{(2/3)\varepsilon_{ij}\varepsilon_{ij}}, \quad i, j = x, y \quad (16)$$

The flowchart in Fig. 4 illustrates the computation procedure for calculating the model-based DIC.

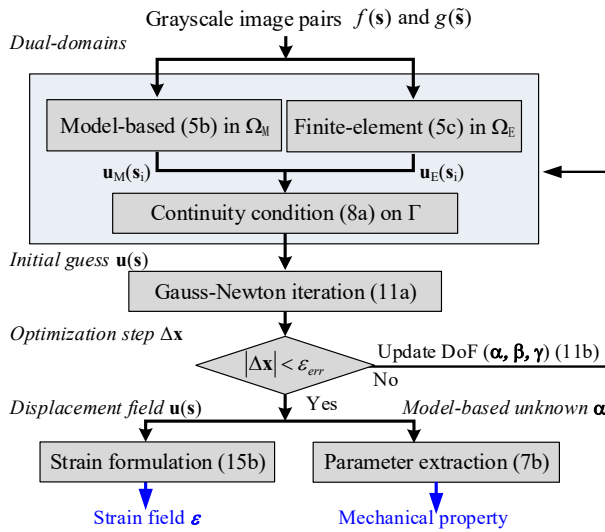


Fig. 4 Flow-chart illustrating the model-based DIC algorithm.

### III. RESULTS AND DISCUSSIONS

The dual-domain method that incorporates a physical-field model to enhance the DIC with FE formulation for high-resolution field-measurements is numerically and experimentally investigated. Table 1 summarizes three most commonly encountered examples to illustrate the dual-domain formulation (1~5) and the algorithm (8~16). Other model-kernel equations can be formulated similarly. Four sets of results are presented: The 1<sup>st</sup> numerically analyzes the effects of the model-kernels on the accuracy and computational time of the displacement field using simulated images, three different DIC methods are compared:

**FE-DIC:** DIC method with global FE meshes.

**M-DIC:** Model-based DIC method with all pixels.

**M-FE-DIC:** Dual-domain method that combines the advantages of the FE-DIC and M-DIC.

Table 1 Model-kernels used in illustration

Example	Application	$\mathbf{H}_M$ (Eq.)	$\boldsymbol{\alpha}$ (Eq.)
1	Rigid Transformation (RT)	(18a)	(18b)
2	Uniaxial tension (UT) of flat plate	(19a)	(19b)
3	UT of flat plate (with a circular hole)	(7a)	(7b)

Illustrated with a uniaxial tensile loading application (Fig. 3) where published experimental results are available for validation, the 2<sup>nd</sup> is a parametric study on the measurements of

the deformed displacement. The 3<sup>rd</sup> numerically analyzes the effects of intensity change and random noise on the measurement errors of the displacement and strain fields. The 4<sup>th</sup> demonstrates the dual-domain method for simultaneously measuring the displacement field and material mechanical properties using published experimental results.

The numerical image pairs are generated by (17a, b) [26]:

$$f(\mathbf{s}) = \sum_{p=1}^{n_p} I_p \exp\left[-(\mathbf{s}-\mathbf{s}_p)^2 / R_p^2\right] \quad (17a)$$

$$g(\tilde{\mathbf{s}}) = \sum_{p=1}^{n_p} I_p \exp\left[-(\mathbf{s}-\mathbf{s}_p-\mathbf{u})^2 / R_p^2\right] \quad (17b)$$

In (17a, b),  $\mathbf{s}_p$  and  $I_p$  are the random coordinates and random intensity of the speckle; the radius  $R_p$  (=4) and total number  $S_p$  (=8000) of speckle were used to generate the pair of images; and the displacement field  $\mathbf{u}$  was extracted from numerical simulation results using FEA software. Written in MATLAB, the Gauss-Newton iteration in model-based DIC was computed on a desktop personal computer (Intel Core i7-3770K, 3.5GHz CPU, 16GB RAM, 64 bits OS). In this study, the grayscale and image gradient on the subpixel location are interpolated with MATLAB biquintic B-splines.

#### A. Rigid transformation and uniaxial tension

For clarity, a flat plate undergoing rigid transformation (RT) and uniaxial tension (UT) is chosen to illustrate the effects of the model-kernels on the accuracy and computational time of the displacement field. Fig. 5 shows a pair of (previous, current) images generated using (17) from the FEA-simulated UT loading with the boundary conditions (BCs) shown in Fig. 5(a). For the RT, the pair of images is related by a subpixel rigid translation ( $u_0=0.5, v_0=0.2$ ) but the prior information is that only transformation occurs. The model kernel  $\mathbf{H}_M$  and unknown  $\boldsymbol{\alpha}$  in  $\mathbf{u}_M = \mathbf{H}_M \boldsymbol{\alpha}$  (5b) for the RT and UT of a flat-plate are given respectively by (18a, b) and (19a, b):

$$\text{RT: } \mathbf{H}_M = \begin{bmatrix} 1 & 0 \\ 0 & 1 \end{bmatrix} \text{ and } \boldsymbol{\alpha} = \begin{bmatrix} u_0 \\ v_0 \end{bmatrix} \quad (18a, b)$$

$$\text{UT: } \mathbf{H}_M(x_i, y_i) = \begin{bmatrix} -x_i & 0 \\ 0 & y_i \end{bmatrix} \text{ and } \boldsymbol{\alpha} = \begin{bmatrix} \nu T / E \\ T / E \end{bmatrix} \quad (19a, b)$$

$\mathbf{H}_M(x_i, y_i)$  can be determined for the  $i^{\text{th}}$  pixel coordinates in  $\Omega_M$  with respect to the plate center. Equation (19b) are similar to (7b) except that the stress on the plate is homogeneous (equal to  $T$ ) for UT loading of a flat plate without a circular hole.

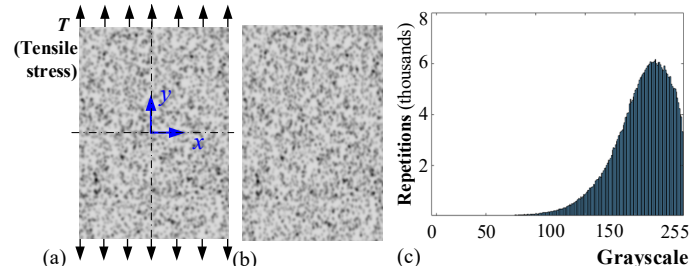


Fig. 5 Numerical generated images (a) Reference (previous) image. (b) Loaded (current) image. (c) Image histogram.

The displacement field ( $u, v$ ) and strains (computed with  $T=1\text{GN}/\text{pixel}$ ,  $E=100\text{GPa}$  and  $\nu=0.3$ ) using the three DIC methods (FE-DIC, M-DIC and M-FE-DIC) are compared in Fig.

6 and in Table 2 where the displacement field accuracy and their computation times are summarized. As shown in Fig. 6(a),  $\Omega_E$  is meshed by 24 quadrilateral elements with size of  $30 \times 30$  pixels;  $\Omega_M$  contains  $180 \times 120$  pixels; and  $\Gamma$  is discretized by seven interfacial nodes for these examples. Equations (18) and (19) are used in both M-DIC and M-FE-DIC. The iteration of (11a) begins with an initial guess where the displacements in both  $\Omega_E$  and  $\Omega_M$  are assumed zero. The matrices in (12b) and (14b, c) are computed with the grayscale and gradient values of the images. The displacement field  $\mathbf{u}$  is obtained when  $\Delta x$  in (11b) is smaller than  $10^{-5}$ .

Table 2 Accuracy and speed of three DIC methods (Examples 1 and 2).

Methods	FE-DIC	M-DIC	M-FE-DIC
% (Max, Ave) Errors	(11.8, 3.3)/ (18.5, 3.7)	(1.6, 0.9)/ (1.9, 1.5)	(6.3, 1.4)/ (6.4, 1.8)
Number of Iterations	14 / 18	4 / 4	5 / 6
Time per Iteration	85ms/91ms	152ms/243ms	94ms/137ms
Computation time	1.20s/1.64s	0.61s/0.97s	0.47s/0.82s

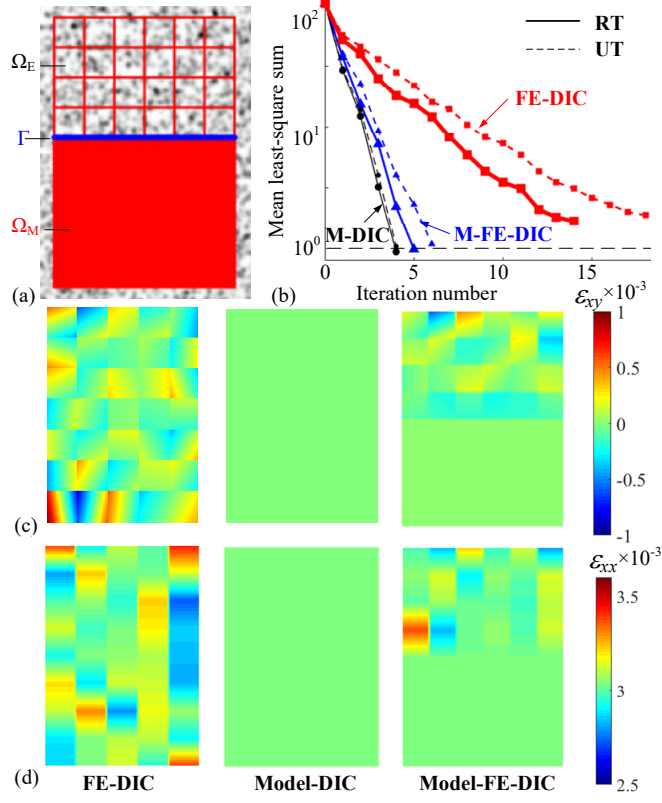


Fig. 6 (a) Effects of FE formulaion and model-kernel on DIC. (a) Subdomains, (b) Number of iterations, (c) Strain in RT, (d) Strain in UT

Some observations can be drawn from the results:

- All three methods are capable of computing the subpixel displacement field in both situations. The model-kernel significantly improves convergence, greatly reducing the global residual between (previous/current) images in the iteration process (Fig. 6b).
- As compared with FE-DIC in Table 2, the maximum (Max) and average (Ave) displacement errors are reduced from (11.8%, 3.3%) to less than (2%, 1%) in M-DIC and (6.3%, 1.4%) in M-FE-DIC with the model kernel (18) in RT. The continuity of the displacement field is satisfied on  $\Gamma$ . The

M-DIC (with fewer DOFs but higher resolution) takes less iterations to converge but more time for each iteration. M-FE-DIC offers a means to relax the trade-off between iteration number and time/iteration, which requires only about 1/3 (in RT) and 1/2 (in UT) of the FE-DIC computation time.

- Because the (whole) image undergoes a rigid-body translation in RT, the measured strain (partial derivatives of the displacement) field should be zero; thus, non-zero strains in Fig. 6(c) are errors in the computed displacement fields and their derivatives. With the BCs in Fig. 5(a),  $\varepsilon_{xx}$  is uniformly equal to the material-related  $vT/E$  for the whole surface. The strain field is uniformly distributed in  $\Omega_M$  in RT and UT because the model-kernel serves as an effective guide; while the errors in  $\Omega_E$  are amplified because the derivatives of  $\mathbf{u}$  must be taken in (15) to calculate strains.

### B. Parametric effects on DIC computation (uniaxial tension)

A numerical study was conducted to investigate the parametric effects on the accuracy of estimated displacements and computation time. In this study, commercial FEA software COMSOL was used to simulate the displacement field around a symmetrical (through-circular-hole) of a thin plate. The BCs for the FEA model are shown in Fig. 7(a) where the upper bound of the thin plate is subjected to a uniaxial tension loading with the prescribed velocity (equivalent to 10 pixels/s); and the lower bound is fixed. The specimen in the simulation was meshed with 2734 free triangular elements. The numerical image sequences are generated using (17a, b) for time-dependent simulations of the displacement fields.

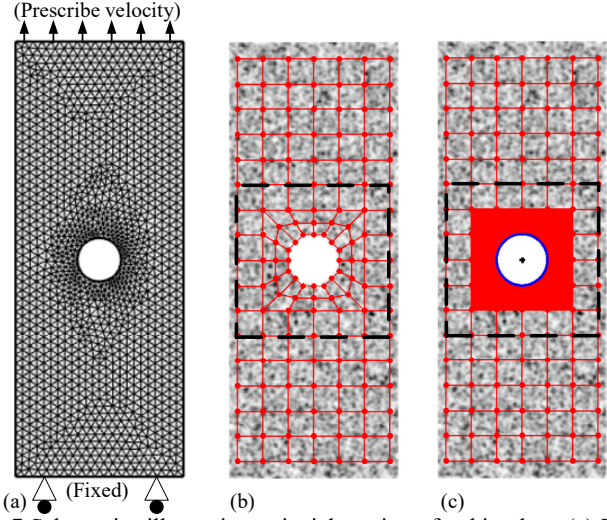


Fig. 7 Schematics illustrating uniaxial tension of a thin plate. (a) FEA BCs. (b) Single-domain FE-DIC. (c) Double-domain M-FE-DIC.

Two different DIC methods (FE-DIC and M-FE-DIC) are compared in Figs. 7(b) and 7(c) respectively, where (60x60 pixel) quadrilateral elements are used in FE-DIC and in  $\Omega_M$ . Additionally, fine elements (25 pixels) are used to model the quadrilateral boundary around the hole in FE-DIC. The M-FE-DIC uses a 240x240-pixel  $\Omega_M$  to model the deformation around the hole. The initial guesses are  $[\beta] = [0]$  in  $\Omega_E$ ,  $\lambda = 0$  on  $\Gamma$ , and  $\alpha = [1 \ 0.3]^T$  for  $\Omega_M$  in (7b). The results are summarized in Figs. 8 to 9 and Table 3.

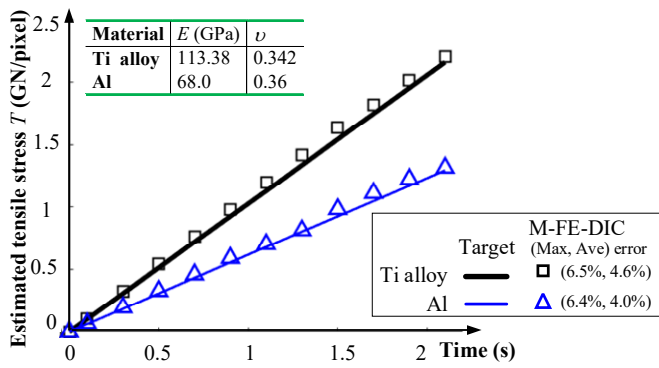


Fig. 8 M-FE-DIC estimated tensile stresses for two different materials.

Fig. 8 compares the estimated tensile stress  $T$  on the upper edge of the plate from the M-FE-DIC for two different materials with known properties ( $E, v$ ); the maximum (Max) and average (Ave) errors of the estimated  $T$  are within 7% and 5% respectively. Fig. 9 graphically illustrates the effect of FE sizes (1<sup>st</sup> row) on the estimated  $u$  and  $v$  displacement fields and their respective errors (2<sup>nd</sup> and 3<sup>rd</sup> rows) defined as

$$(u_{\text{error}}, v_{\text{error}}) = (u, v)_{\text{DIC}} - (u, v)_{\text{COMSOL}}$$

Four mesh types (1<sup>st</sup> row) are used to iteratively compute (11) for the same  $\Omega_M$ . The rectangles bound by blacked dash-line in Figs. 7(b, c) were extracted to investigate the effects of element size for the DIC measurement. The hole radius ( $a = 52$  pixels) was estimated using Hough transform method. The computation time are compared in Table 3.

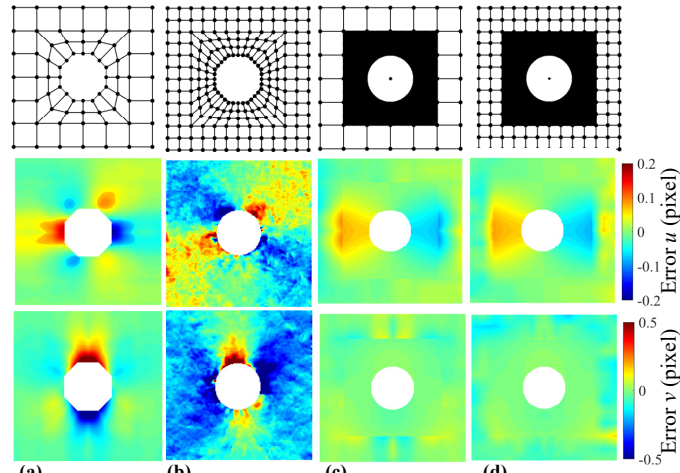


Fig. 9 Effect of element sizes on displacement measurement. (a) Coarse FE-DIC. (b) Fine FE-DIC. (c) Coarse M-FE-DIC and Fine M-FE-DIC.

As simulated in Fig. 9, coarse FE-DIC (1<sup>st</sup> column) with large elements cannot capture the complex displacement around the hole, where maximum errors of both  $u$  and  $v$  can be observed near the center-hole region. Fine meshes in FE-DIC (2<sup>nd</sup> column) lead to a smooth displacement field at the expense of high computation time (more than 6 minutes), but with low accuracy for the whole surface because smaller elements contain little image information for image correlation.

Table 3 Iteration and computation time of different DIC methods.

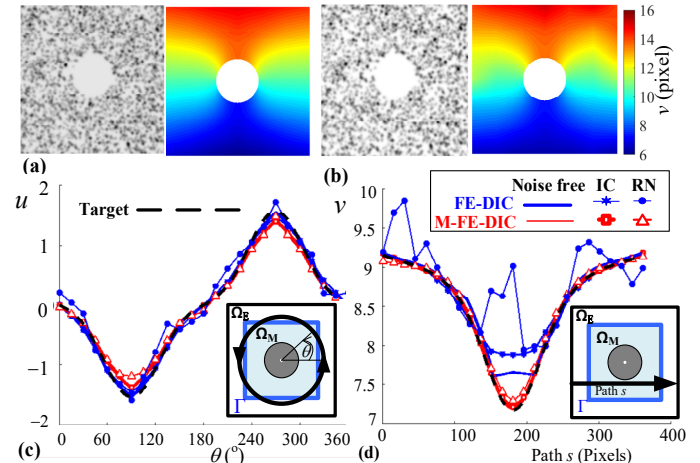
Methods	FE-DIC		M-FE-DIC	
Mesh	Coarse	Fine	Coarse	Fine
No. of unknowns	176	504	116	310
No. of iteration	109	287	24	58
Computation time	114.6s	382.1s	35.9s	94.1s

With the model-kernel (7a) for an infinite plate, the dual-domain M-FE-DIC (3<sup>rd</sup> and 4<sup>th</sup> column) offers an effective means to reconstruct the complex deformation fields around the hole, while the far-field displacements are adequately captured by coarse or fine FE formulation which has little effect on the displacement field in  $\Omega_M$ . The continuity condition of the displacement field is well satisfied on the rectangular interface. The model-kernel in  $\Omega_M$  greatly reduces the number of iterations and computation time. It is worth noting that since (7a) is formulated for calculating the displacement around the circular hole in an infinite plate, errors are expected near the edge boundary far from the hole. The dual-domain formulation creatively makes full use of the model-kernel in  $\Omega_M$  where (7a) is valid leaving the un-modeled  $\Omega_E$  to FE formulation.

### C. Noise effect in simulated uniaxial tension

The robustness against light intensity changes (IC) and random noise (RN) on the estimated displacement field (Fig. 10) and strain field (Fig. 11) was investigated numerically. Fig. 10(a) shows the “current” image with a 10% intensity reduction from the noise-free “previous” image and its corresponding  $v$ -component of the displacement field reconstructed using M-FE-DIC. Similarly, the “current” image contaminated by a zero-mean Gaussian noise and its M-FE-DIC reconstructed  $v$ -component field are shown in Fig. 10(b). The Gaussian noise contaminated image was simulated with (20) where  $\varepsilon_p$  is the random grayscale error associated with the  $p^{\text{th}}$  speckle with displacement  $\mathbf{u}$  and  $\sigma (= 0.05I_p)$  is a standard deviation:

$$g(\tilde{\mathbf{s}}) = \sum_{p=1}^{n_p} \left\{ \left[ I_p + \varepsilon_p(\mu, \sigma) \right] \exp \left[ -\frac{(\mathbf{s} - \mathbf{s}_p - \mathbf{u})^2}{R_p^2} \right] \right\} \quad (20)$$

Fig. 10 Effects of IC and RN contamination on estimated displacement fields. (a) IC image with 10% intensity reduction and its reconstructed  $v$  field. (b) RN image and its reconstructed  $v$  field. (c) Displacement  $u$  along the circular path. (d) Displacement  $v$  along the horizontal path  $s$ .

For quantitative visualization, the  $u$  displacement along a circle (with a 125-pixel radius) and the  $v$  displacement along a horizontal line (65 pixels below the hole-center), which pass through both  $\Omega_M$  and  $\Omega_E$  regions are respectively plotted in Figs. 10(c) and 10(d) where FE-DIC was calculated with coarse meshes (1<sup>st</sup> column in Fig. 9). Quantitative effects of the light changes and random noise on the DIC are compared in Table 4.

Table 4 Effects of intensity and noise on absolute (Max, Ave) errors.

Image Noise type Grayscale (Ave, SD)	Previous Noise-free (210.1, 34.6)	Current image	
	IC (189.2, 31.1)	RN (207.8, 36.9)	
FE-DIC (Max, Ave)	$ \Delta u $ (pix)	(0.38, 0.05)	(0.41, 0.03)
	$ \Delta v $ (pix)	(0.82, 0.06)	(0.81, 0.05)
	$ \Delta \varepsilon_x $ (%)	(0.75, 0.09)	(1.05, 0.10)
	$ \Delta \varepsilon_y $ (%)	(1.81, 0.12)	(2.14, 0.13)
	$ \Delta \varepsilon_{xy} $ (%)	(1.20, 0.12)	(1.64, 0.10)
M-FE-DIC (Max. Ave)	$ \Delta u $ (pix)	(0.13, 0.04)	(0.14, 0.05)
	$ \Delta v $ (pix)	(0.08, 0.01)	(0.09, 0.02)
	$ \Delta \varepsilon_x $ (%)	(0.66, 0.08)	(0.68, 0.08)
	$ \Delta \varepsilon_y $ (%)	(0.82, 0.04)	(0.87, 0.04)
	$ \Delta \varepsilon_{xy} $ (%)	(0.96, 0.06)	(0.98, 0.06)

Fig. 11(a) shows the COMSOL-simulated strain fields ( $\varepsilon_y$  and  $\varepsilon_{xy}$ ) as a basis for numerical verification of the reconstructed strain fields by using the FE-DIC (Fig. 11b) and M-FE-DIC (Fig. 11c) methods, where the strain tensor was calculated from (15). To gain insights into the effect of the DIC methods on the reconstructed strain distributions, Fig. 11(d) compares the ( $\varepsilon_y$  and  $\varepsilon_{xy}$ ) strains along a circular path, which were computed by taking the derivatives of the displacements in (Fig. 10c). Fig. 11(e) shows the effects of IC and RN on the strain fields, where the results from two reconstruction methods are compared.

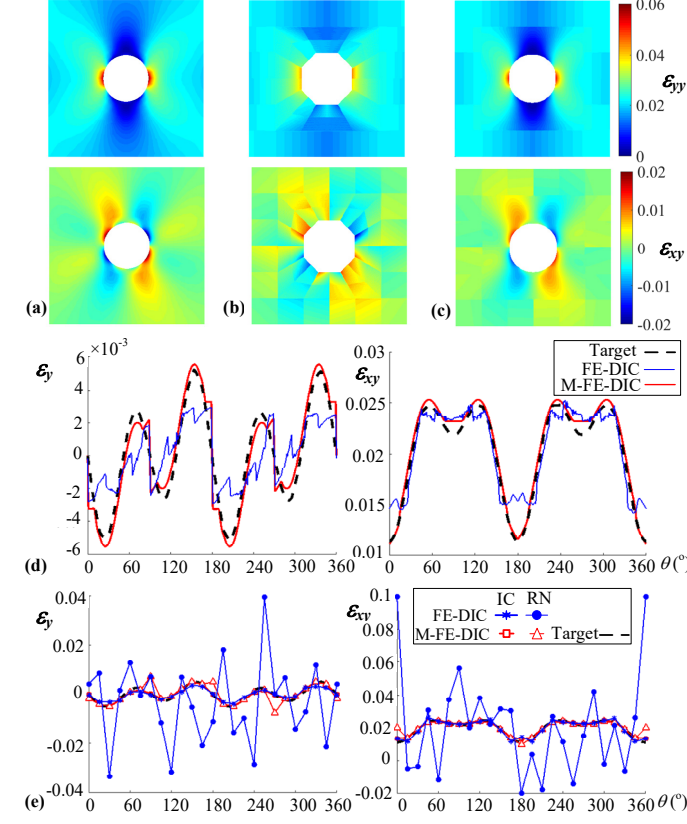


Fig. 11 Effects of IC and RN contamination on estimated strain fields: (a) COMSOL simulations (b) FE-DIC reconstruction. (c) M-FE-DIC reconstruction. Reconstructed strain distribution along the circular line: (d) Noise-free images. (e) Noise-contaminated images.

Some observations can be drawn from Figs. 10 and 11 and Table 4:

- Both DIC methods are capable of measuring small deformation (Fig. 10c), but FE-DIC underestimates the large

deformation (Fig. 10d). In the absence of RN, M-FE-DIC accurately estimates the displacement and strain fields with maximum errors of less than 0.15-pixel in displacement (Fig. 10c, d) and 1% in strain (Fig. 11d).

- From the comparison between the two columns (noise-free and IC) in Table 4 where the displacements ( $|\Delta u|$  and  $|\Delta v|$ ) and strains ( $|\Delta \varepsilon_x|$   $|\Delta \varepsilon_{xy}|$   $|\Delta \varepsilon_y|$ ) are the absolute differences between the DIC measurements and their respective simulated targets, IC have little effects on the reconstructed displacements because of the normalized correlation criterion (2a).
- As compared with the noise-sensitive FE-DIC which fails in the presence of random noise (Table 4, column RN), the model-kernel in M-FE-DIC effectively suppresses the Gaussian noise effects as demonstrated in Figs. 10(c, d) and 11(e) and in the last column (RN) of Table 4, reducing the (Max, Ave) absolute discrepancies from (14.5, 0.59) to (1.19, 0.12) pixels in  $v$  displacements, and two orders of maximum errors in strain (to within 2.5%).
- The displacement and strain fields reconstructed by using M-FE-DIC are smoother than FE-DIC, particularly in the presence of noise. Discontinuities are observed at the boundaries across elements in FE-DIC because the 4-node quadrilateral is a  $C^0$  continuous element, which can be further improved by implementing the  $C^1$  elements in FE formulation.

#### D. Uniaxial tension (UT) experiment

With the model-kernel in  $\Omega_M$ , the material ( $E, \nu$ ) as well as the displacement and strain fields can be simultaneously can be determined from experimentally measured tensile force as a function of the longitudinal change (clamp-displacement in the  $v$  direction) as inputs. For illustrating this practicality, experimentally obtained published images [27] (consisting of one “previous” and 10 sequential “current” 420×1040-pixel images) for similar UT loading were used to validate the M-FE-DIC method and demonstrate its effectiveness. Since the material properties and loading tensile force are not recorded in this database [27], published data (specimen geometry and loading force) in a similar experiment were used in the following M-FE-DIC measurement. The specimen was a 22.5mm-width plate made of aluminum-glass laminate (a common material for the tension specimen) with a 8mm-diameter hole; the length and thickness of the specimen are 100mm and 3.1mm respectively.

Subdomains and model-based coordinates (with its origin defined at the hole-center) for the M-FE-DIC are similar in Fig. 7(c). Using Hough transform, the hole-radius was found to be 54 pixels suggesting 6.75pixels/mm for mapping the image into real physical length. The dual-domain was formulated with 90 rectangle elements (50×50 pixels each) in  $\Omega_E$ , and the model domain  $\Omega_M$  (200×300 pixels) around the center-hole. The Lagrangian multiplier  $\lambda$  is discretized by 20 interfacial nodes. Once  $(\alpha_1, \alpha_2)$  are determined from M-FE-DIC, the Poisson ratio  $\nu$  (that does not depend on the input loading force) of the target specimen material can be estimated from the ratio  $\alpha_2/\alpha_1$  (7b). Similarly, the Young’s modulus  $E$  can be identified in terms of

the measured tensile force (7b) for a given hole-radius  $a$ .

The results for the whole deformation process are illustrated in Fig. 12. Figs. 12(a, b) graph the  $v$ -displacement and equivalent-strain  $\varepsilon_{eq}$  (16) computed from the sequences of the odd-numbered (3, 5, 7, 9, 11) images. As demonstrated in Fig. 12(a, b), the characteristic X-shape strain localization occurred around the hole can be monitored during the deformation process. The estimated mechanical properties the (target) material are compared in Fig. 12(c, d) where the dash-lines are published experimental measurements;  $E = 12.33\text{GPa}$  and  $\nu = 0.198$  [28]. As seen in Fig. 12(c), a consistent value of  $\nu=0.2$  was determined, which agrees well with the published data. In Fig. 12(b),  $E$  is reasonably estimated within relative errors of less than 5% of the published data.

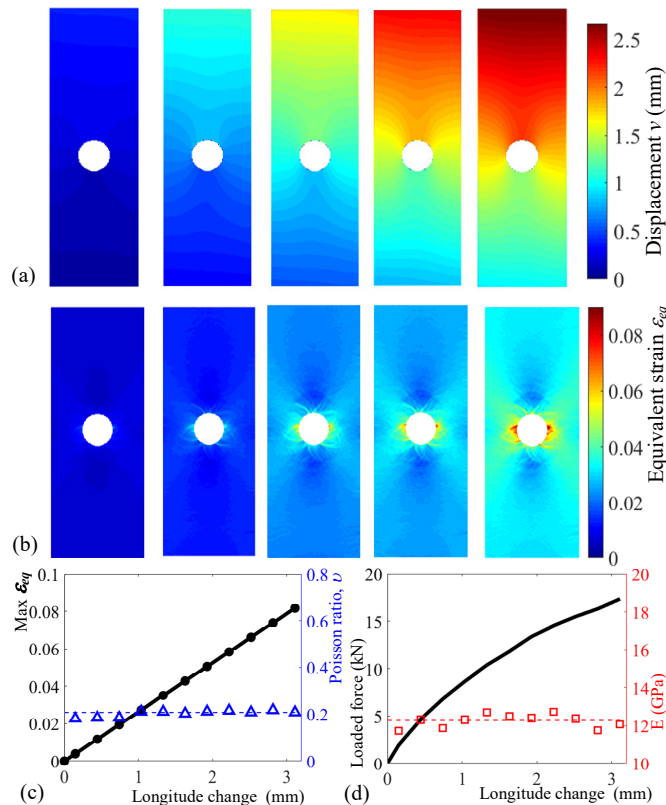


Fig. 12 Simultaneous measurements in tensile test. (a) Displacement. (b) Equivalent strain field. (c) Poisson ratio. (d) Young's modulus.

#### IV. CONCLUSION

The dual domains (physics-based model and FE-based region) of the proposed global-DIC method have been formulated, along with the interfacial and continuity conditions, to solve the global displacement field and simultaneously estimate the mechanical properties of the deformed material in a single calculation. The effectiveness of the dual-domain global DIC method has been evaluated by comparing the DIC reconstructed displacement/strain fields and estimated parameters against targets simulated using the commercial FEA software COMSOL, and with published experimental data.

The proposed method has been numerically illustrated with two examples; rigid translation and uniaxial tensile loading. Three methods (FE-DIC, M-DIC and M-FE-DIC) are compared; results demonstrate that M-FE-DIC is superior in terms of computational efficiency and accuracy. The dual-domain DIC

provides an effective means to constrain the solutions to the iterative minimization of the DIC criterion, leading to a faster convergence and requiring only 1/3 time of the FE-DIC computation without sacrificing the displacement accuracy. More importantly, unlike FE-DIC which fails in the presence of random noise, the model-kernel in M-FE-DIC effectively suppresses the Gaussian noise effects, which reduces the absolute errors to 1/5 in displacement and 1/40 in strain field.

While the M-FE-DIC method that combines a physics-based model and FE-DIC has been illustrated in the context of 2D in-plane deformation, it can be extended to enhance StereoDIC (or 3D-DIC) which have seen emerging growth in biomedical applications [8] when an appropriate 3D model along with stereo and/or multi-view images for available for reconstruction of the 3D displacement/strain fields; for example [29].

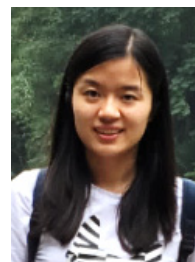
#### REFERENCES

- [1] M. A. Sutton, J.-J. Orteu, and H. W. Schreider, *Image correlation for shape, motion and deformation measurements: basic concepts, Theory and Applications*, USA, Springer, 2009.
- [2] T. Kreis, "Application of digital holography for nondestructive testing and metrology: A review," *IEEE Trans. Ind. Informat.*, vol. 12, no. 1, pp. 240-247, 2016.
- [3] X. Li, W. Xu, M. A. Sutton, and M. Mello, "In situ nanoscale in-plane deformation studies of ultrathin polymeric films during tensile deformation using atomic force microscopy and digital image correlation techniques," *IEEE Trans. Nanotechnol.*, vol. 6, no. 1, pp. 4-12, 2007.
- [4] S. von Enzberg and A. Al-Hamadi, "A multiresolution approach to model-based 3-D surface quality inspection," *IEEE Trans. Ind. Informat.*, vol. 12, no. 4, pp. 1498-1507, 2016.
- [5] J. Lei, J. Sun, Z. Pan, S. Kwong, J. Duan and C. Hou, "Fast mode decision using inter-view and inter-component correlations for multiview depth video coding," *IEEE Trans. Ind. Informat.*, vol. 11, no. 4, pp. 978-986, 2015.
- [6] Y. Guo, W. D. Compton and S. Chandrasekar, "In situ analysis of flow dynamics and deformation fields in cutting and sliding of metals," *Proc. R. Soc. A*, vol. 471, no. 2178, 2015.
- [7] M. Jerabek, Z. Major and R. Lang, "Strain determination of polymeric materials using digital image correlation," *Polym. Test.*, vol. 29, pp. 407-416, 2010.
- [8] D. Solav, K. M. Moerman, A. M. Jaeger, K. Genovese and H. M. Herr, "MultiDIC: An open-source toolbox for multi-view 3D digital image correlation," *IEEE Access*, vol. 6, pp. 30520-30535, 2018.
- [9] B. Pan, "Recent progress in digital image correlation," *Exp. Mech.*, vol. 51, no. 7, pp. 1223-1235, 2011.
- [10] J. Blaber, B. Adair, and A. Antoniou, "Ncorr: open-source 2D digital image correlation matlab software," *Exp. Mech.*, vol. 55, no. 6, pp. 1105-1122, 2015.
- [11] G. Besnard, F. Hild, and S. Roux, "Finite-element displacement fields analysis from digital images: application to portevin-le chatelier bands," *Exp. Mech.*, vol. 46, no. 6, pp. 789-803, 2006.
- [12] M. Bornert, F. Bremand, P. Doumalin, J.-C. Dupre, M. Fazzini, M. Grediac, F. Hild, S. Mistou, J. Molimard, J.-J. Orteu, L. Robert, Y. Surrel, P. Vacher and B. Wattrisse, "Assessment of digital image correlation measurement errors: methodology and results," *Exp. Mech.*, vol. 49, no. 3, pp. 353-370, 2009.
- [13] F. Hild and S. Roux, "Digital image correlation: from displacement measurement to identification of elastic properties—a review," *Strain*, vol. 42, pp. 69-80, 2006.

- [14] S. Ma, Z. Zhao and X. Wang, "Mesh-based digital image correlation method using higher order isoparametric elements," *J. Strain Anal. Eng.*, vol. 47, no. 3, pp. 163–175, 2012.
- [15] L. Wittevrongel, D. Debruyne, S. V. Lomov and P. Lava, "Implementation of convergence in adaptive global digital image correlation," *Exp. Mech.*, vol. 56, no. 5, pp. 797–811, 2016.
- [16] J.-C. Passieux, F. Bugarin, C. David, J.-N. Perie and L. Robert, "Multiscale displacement field measurement using digital image correlation: Application to the identification of elastic properties," *Exp. Mech.*, vol. 55, pp. 121–137, 2015.
- [17] A. S. Wu, D. W. Brown, M. Kumar, G. F. Gallegos and W. E. King, "An experimental investigation into additive manufacturing-induced residual stresses in 316L stainless steel," *Metall. Mater. Trans. A*, vol. 45, no. 13, pp. 6260–6270, 2014.
- [18] Z. Tomičević, F. Hild and S. Roux, "Mechanics-aided digital image correlation," *J. Strain Anal. Eng.*, vol. 48, no. 5, pp. 330–343, 2013.
- [19] V. Blanz and T. Vetter, "Face recognition based on fitting a 3D morphable model," *IEEE Trans. Pattern. Anal. Mach. Intell.*, vol. 25, no. 9, pp. 1063–1074, 2003.
- [20] M. R. Sabuncu, B. T. T. Yeo, K. Van Leemput, B. Fischl and P. Golland, "A generative model for image segmentation based on label fusion," *IEEE Trans. Med. Imaging*, vol. 29, no. 10, pp. 1714–1729, 2010.
- [21] X. Wang, Z. Pan, F. Fan, J. Wang, Y. Liu, S. X. Mao, T. Zhu, and S. Xia, "Nanoscale deformation analysis with high-resolution transmission electron microscopy and digital image correlation," *J. Appl. Mech.*, vol. 82, pp. 121001–121001-9, 2015.
- [22] B. Pan, H. Xie and Z. Wang, "Equivalence of digital image correlation criteria for pattern matching," *Appl. Opt.*, vol. 49, no. 28, p. 5501, 2010.
- [23] M. H. Sadd, *Elasticity: theory, applications, and numerics*, 3rd ed., Amsterdam, Boston, USA, Elsevier, 2014.
- [24] M. Hazewinkel, *Encyclopaedia of Mathematics*. Springer Science & Business Media, 2013.
- [25] J.-C. Passieux, A. Gravouil, J. Réthoré, and M.-C. Baietto, "Direct estimation of generalized stress intensity factors using a three-scale concurrent multigrid X-FEM," *Int. J. Numer. Meth. Eng.*, vol. 85, no. 13, pp. 1648–1666, 2011.
- [26] P. Zhou and K. E. Goodson, "Subpixel displacement and deformation gradient measurement using digital image speckle correlation," *Opt. Eng.*, vol. 40, no. 8, pp. 1613–1620, 2001.
- [27] P. Reu, M. Iadicola and B. Blaysat (2018), Society for experimental mechanics. [online] Sem.org. Available at: <https://sem.org/dic-challenge> [Accessed 24 Sep. 2018].
- [28] T. A. Barreto and R. C. Santiago, "Experimental study of the tensile strength of open-hole fiber-metal laminates," *Proc. of BCCM on Compos. Mater.*, Brazil, July 22–25, 2018.
- [29] J. Ji, Y. Xie and K.-M. Lee, "Coupled Multi-view Vision and Physics-based Synthetic Perception for 4D Displacement Field Reconstruction," *IEEE/ASME Trans. on Mechatronics*, vol. 21, no. 2, pp. 980–992, 2016.



**Yang Huang** received the B.S. degree in material processing engineering from Huazhong University of Science and Technology, Wuhan, China, in 2013. Currently, he is a Ph.D. candidate in School of Mechanical Science and Engineering at Huazhong University of Science and Technology, Wuhan, China. His research interests include image-based sensing, thermal field reconstruction, and machining modeling.



**Jingjing Ji** (M'14) received the B.S. and Ph.D. degrees in mechanical engineering from Zhejiang University, Hangzhou, China, in 2008 and 2014, respectively.

She is currently an Associate Professor with the State Key Laboratory of Digital Manufacturing Equipment and Technology, School of Mechanical Science and Engineering, Huazhong University of Science and Technology, Wuhan, China. Her research interests include mechatronics, robotics, design, modeling and field reconstruction.



**Kok-Meng Lee** (M'89–SM'02–F'05) received the B.S. degree in mechanical engineering from the State University of New York, Buffalo, NY, USA, in 1980, and the S.M. and Ph.D. degrees in mechanical engineering from the Massachusetts Institute of Technology, Cambridge, MA, USA, in 1982 and 1985, respectively.

He is currently a Professor with the George W. Woodruff School of Mechanical Engineering, Georgia Institute of Technology, Atlanta, GA, USA. He is also a Distinguished Professor with the State Key Laboratory of Digital Manufacturing Equipment and Technology, Huazhong University of Science and Technology, Wuhan, China. His research interests include system dynamics/control, robotics, automation, and mechatronics. He holds eight patents in machine vision, three degrees-of-freedom spherical motor/encoder, and live-bird handling system.

Dr. Lee is a fellow of the American Society of Mechanical Engineers (ASME). He is the founding Editor-in-Chief of Springer International Journal of Intelligent Robotics and Applications. He received the National Science Foundation Presidential Young Investigator, the Sigma Xi Junior Faculty Research, the International Hall of Fame New Technology, the Kayamori Best Paper Awards, the TMech Best Paper Award, and the Michael J. Rabin Leadership Award. He was also honored as a Pao Yu-Kong Chair Professor at Zhejiang University, Hangzhou, China.